Integrated Uncertainty/Disturbance Compensation With Second-Order Sliding-Mode Observer for PMLSM-Driven Motion Stage

Rui Yang, Mingyi Wang, Liyi Li, *Senior Member, IEEE*, Yiming Zenggu, and Jialin Jiang

***Abstract*—The permanent magnet linear synchronous machine driven motion stage for the semiconductor manufacturing equipment and machine tools has the basic requirement of high-dynamic response and high position accuracy. However, due to the direct-drive structure, the effect of parameter uncertainty, including the electrical and the mechanical one, and external disturbance will be directly exerted to the stage. In this paper, an integrated compensation scheme of the overall uncertainty and disturbance is proposed based on the second-order sliding-mode observer (SOSMO). First, an extended state model for considering the disturbance dynamics is established for both the electrical and the mechanical subsystems. To obtain high-dynamic current performance, the predictive current control (PCC) is utilized to design the current controller, and the SOSMO is integrated to compensate the main problem of a parameter mismatch for the PCC. Furthermore, the SOSMO is also configured to estimate the force ripple, and then the observation term is applied in parallel to the velocity controller. With this integrated scheme, the disturbance of the motion stage can be simply and effectively compensated. Experiments are demonstrated to show the effectiveness of the integrated method on both the PCC and force ripple suppression.**

***Index Terms*—Force ripple, permanent magnet linear synchronous machines (PMLSMs), predictive current control (PCC), second-order sliding-mode observer (SOSMO), uncertainty/disturbance.**

I. Introduction

WITH the increasing demand for the high-velocity/high-precision linear motion systems, the permanent magnet linear synchronous machines (PMLSMs) have been widely applied to the precision applications [1], [2], such as the semiconductor manufacturing equipment and the computer numerical controlled machine tools. The superior advantages

Manuscript received January 10, 2018; revised March 10, 2018, April 23, 2018, and May 31, 2018; accepted June 4, 2018. Date of publication June 7, 2018; date of current version February 5, 2019. This work was supported in part by the State Key Program of National Natural Science of China under Grant 51537002, in part by the National Natural Science of China Youth Fund under Grant 51707046, and in part by the State Major Program of National Natural Science of China under Grant 51690182. Recommended for publication by Associate Editor A. J. M. Cardoso. *(Corresponding author: Mingyi Wang.)*

The authors are with the School of Electrical Engineering and Automation, Harbin Institute of Technology, Harbin 150001, China (e-mail:

the resistance [13]. Indirectly, the effect of parameter uncertainty and unmodeled dynamics were considered as lumped disturbance first, and then the disturbance estimation/observation methods combined with the feedforward compensation were applied to suppress its influence, e.g., the time delay control method [14], the adaptive method [15], the Luenberger observer method [16], the extended Kalman filter method [17], and the sliding-mode-observer method [9], [18], [19]. The lumped disturbance is actually coupled with the system states, i.e., the currents and the velocity, especially under high-velocity/high-dynamic operation conditions. However, the methods presented in [14]–[16] and [18] were implemented based on the assumption that the disturbance was varying slowly; thus, it was more or less inaccurate.

Second, for the motion systems, both the mechanical parameter uncertainty and the external force ripple exist in the mechanical subsystem. The relative control methods for suppressing their influence can also be classified into two categories. One is improving the control strategies, such as the repetitive control [20], the iterative learning control [21], the adaptive robust control [22], and the periodical adaptive disturbance observer (DOB) [1]. These methods can effectively improve the position tracking accuracy, but there exist disadvantages of consuming more storage space or requiring a more complex control algorithm. The idea of the other one is the same as the indirect method for disturbance compensation of the PCC, i.e., observation first and then compensation. In [23], an adaptive force ripple feedforward method based on its fundamental component was proposed. However, the force ripple is nonlinear and nonperiodical about the position in reality [22], and thus it cannot be accurately compensated. The simple DOB was utilized to estimate the detent force in [24] and [25] without considering its characteristic, but the filter cutoff-frequency must be balanced between the observation accuracy and the noise rejection capability, so the force ripple cannot be suppressed in all velocity ranges. In [4] and [26], the Jacobian linear observer was designed to estimate and compensate the force ripple, where the fast convergence speed and accurate estimation can be obtained; however, the high-frequency components and the nonlinear external disturbance cannot be included. Therefore, the force ripple estimation results of the above-mentioned methods were not accurate in all frequency ranges.

Instead of assuming that the disturbance is slowly varying, Zhang *et al.* [9] and Guermouche *et al.* [27] proposed to model the disturbance as an extended state, then the disturbance dynamic can also be considered. Recently, the higher order sliding mode has attracted wide attention, of which the main advantages lie in its chattering reduction effect, higher control accuracy, and its maintained invariance feature to external disturbance [28], [29]. Here, *one of the main focuses of this paper* is to combine the method of the extended state [9], [27] with the second-order sliding-mode observer (SOSMO) based on the supertwisting algorithm presented in [28] and [29] to obtain more accurate disturbance estimation. *The other focus of this paper* is the design method for integrated uncertainty/disturbance observation and compensation with SOSMO, where the application of SOSMO will be exploited further from the single current loop to the overall velocity–current closed-loop, and then the overall disturbance of the electrical and mechanical subsystems can be suppressed simultaneously. A variable-gain adaptive method has been proposed in our previously published paper [31], but the main aim is inductance robustness improvement. Meanwhile, the basic theories and the main motivations are different in this paper.

The remainder of this paper is organized as follows. In Section II, the system description is presented, and the problem statement is discussed. The uncertainty/disturbance observation and compensation method based on the SOSMO is introduced in Section III. In Section IV, the validity of the proposed design method is evaluated with experiments. Conclusions are given in Section V.

II. System Description and Problem Formulation

In this paper, the motion stage driven by the surface-mounted PMLSM is investigated. For more accurate modeling of the entire system, both the electrical and mechanical dynamics are considered as follows.

A. Electrical Dynamics

In the synchronous rotating frame (dq-axis), the electrical dynamics of the PMLSM can be described with the voltage equations, where the basic motor parameters are needed. However, from the point of practical application, the motor parameters cannot be precisely measured online or even offline. Using the nominal system parameters, the dynamics of the PMLSM considering both the disturbance caused by parameters variation and unmodeled dynamics can be described as [12]

$$\left.\begin{aligned} u_d &= R_{\rm so} i_d + L_{\rm so}\tfrac{d}{dt} i_d - \tfrac{\pi}{\tau} p v L_{\rm so} i_q + f_d \\ u_q &= R_{\rm so} i_q + L_{\rm so}\tfrac{d}{dt} i_q - \tfrac{\pi}{\tau} p v L_{\rm so} i_d + \tfrac{\pi}{\tau} p v \psi_{fo} + f_q \end{aligned}\right\} \quad (1)$$

where u_d *and* u_q are the applied d- and q-axis stator voltages, respectively, i_d *and* i_q are the d- and q-axis components of the stator currents, respectively. R_s and L_s denotes the stator resistance and inductance, respectively. ψ_f represents the permanent-magnet flux linkage. v is the linear velocity of the mover, τ is the pole pitch, and p is the number of pole pairs. The subscript "o" denotes the nominal values, and f_d and f_q represent the lumped disturbances due to the parameters variation and the unmodeled dynamics, and they can be given by

$$\left.\begin{aligned} f_d &= \Delta R_s i_d + \Delta L_s \tfrac{d}{dt} i_d - \tfrac{\pi}{\tau} p v \Delta L_s i_q + \varepsilon_d \\ f_q &= \Delta R_s i_q + \Delta L_s \tfrac{d}{dt} i_q + \tfrac{\pi}{\tau} p v \Delta L_s i_d + \tfrac{\pi}{\tau} p v \Delta \psi_f + \varepsilon_q \end{aligned}\right\} \quad (2)$$

where $\Delta R = R_s - R_{\rm so}, \Delta L = L_s - L_{\rm so}, \Delta\psi_f = \psi_f - \psi_{f_o}$, and ε_d and ε_q are the lumped unmodeled dynamics of d- and q-axis, respectively.

According to (2), we can observe that the disturbance is coupled with the system states, i.e., the currents i_{dq} and the velocity v. Taking into account the desired and actual high-dynamic response of the inner current loop and the special high-velocity operation requirement of the PMLSMs, the time derivatives of the disturbance cannot be simply assumed to be zero, i.e.,

$\dot{f}_{dq} \neq 0$. Therefore, considering the disturbance dynamics is necessary. Rearranging (1) in the state-space form, the current dynamics of the motor can be represented as

$$\left.\begin{aligned} \dot{\boldsymbol{i}} &= \boldsymbol{g}_0(\boldsymbol{i}, v) + \tfrac{1}{L_{\rm so}}(\boldsymbol{u}_1 - \boldsymbol{f}) \\ \dot{\boldsymbol{f}} &= \boldsymbol{h}(\boldsymbol{i}, v) \\ \boldsymbol{y}_1 &= \boldsymbol{i} \end{aligned}\right\} \tag{3}$$

where the variables $\boldsymbol{i}$, the inputs $\boldsymbol{u}_1$, the disturbance $\boldsymbol{f}$, and the nonlinear function $\boldsymbol{g}_0(\boldsymbol{i}, v)$ are defined as follows:

$$\boldsymbol{i} = [\, i_d \;\; i_q \,]^T, \boldsymbol{u}_1 = [\, u_d \;\; u_q \,]^T, \boldsymbol{f} = [\, f_d \;\; f_q \,]^T$$

$$\boldsymbol{g}_0(\boldsymbol{i}, v) = \begin{bmatrix} -\frac{R_{\rm so}}{L_{\rm so}} i_d + \frac{\pi}{\tau} p v i_q \\ -\frac{R_{\rm so}}{L_{\rm so}} i_q - \frac{\pi}{\tau} p v i_d - \frac{\pi}{\tau} p v \frac{\psi_{fo}}{L_{\rm so}} \end{bmatrix}$$

here, the expression $\boldsymbol{h}(\boldsymbol{i}, v)$ denotes the relation among the change rate of the disturbance and the system states, and $\boldsymbol{y}_1$ is the output of the electrical subsystem.

B. Mechanical Dynamics

Under the $i_d^* = 0$ vector control strategy, the output thrust of the surface-mounted PMLSM can be simply given as [1]

$$F_e(t) = \frac{3\pi}{2\tau} p \psi_f i_q = K_f i_q \tag{4}$$

where $K_f = \frac{3\pi}{2\tau} p \psi_f$ denotes the thrust coefficient of the motor.

Similarly, using the nominal system parameters, the mechanical dynamics of the PMLSM-driven motion stage with force ripple and external disturbance can be given as

$$\left.\begin{aligned} \tfrac{d}{dt} x &= v \\ M_o \tfrac{d}{dt} v &= F_{eo} - F_{\rm dis} \end{aligned}\right\} \tag{5}$$

where x is the position of the mover, M is the mass of all the moving part, $F_{eo}(t) = K_{fo} i_q$ is the desired nominal output thrust, F_{dis} represents the total effect of parameter uncertainty and external force, and it can be described as

$$\begin{aligned} F_{\rm dis} = & -\Delta K_f i_q + \Delta M \tfrac{d}{dt} v + B v \\ & + F_r(x) + F_{\rm ext}(x, v) + \varepsilon_F \end{aligned} \tag{6}$$

where $\Delta K_f = K_f - K_{fo}$ [which is equivalent to the flux variation $\Delta\psi_f = \psi_f - \psi_{fo}$ according to (4)], $\Delta M = M - M_o$, B is the viscous friction coefficient and can be neglected for the air-bearing stage in this paper, $F_{ext}(x, v)$ represents the external force including the cable force and the load force, and ε_F denotes the effect of the unmodeled mechanical dynamics, $F_r(x)$ is the ripple force of the linear motor comprises detent force, the effect of flux and current distortions, and the influence of current offsets [25], and it can be modeled as a nonlinear position-dependent periodical function with [22]

$$F_r(x) = \sum_{n=1}^{\infty} f_n(x) \cos(\tfrac{n\pi}{\tau} x + \delta_n) \tag{7}$$

where $f_n(x)$ and δ_n are the amplitude and initial electrical angle of the corresponding n th-order harmonic, respectively.

Instead of modeling each part of the mechanical disturbance, the overall parameter uncertainty and external force are taken as a lumped disturbance $F_{\rm dis}$. For simplification, the system (5) can be rearranged as a perturbed double-integrator with

$$\left.\begin{aligned} \dot{x} &= v \\ \dot{v} &= u_2 + \rho_d \\ \dot{\rho}_d &= h_{\rho_d} \end{aligned}\right\} \tag{8}$$

where $u_2 = \frac{1}{M_o} K_{fo} i_q$, $\rho_d = -\frac{1}{M_o} F_{\rm dis}$, and h_{ρ_d} are the control input, the disturbance, and its derivative term, respectively.

C. Overall Systems

The mechanical and electrical subsystems are linked through the electromagnetic thrust, while both the effective thrust and the harmful disturbance are exerted to the moving part directly without any buffer, since the transmission link is eliminated. Combining (3) with (8), the entire motion system can be modeled in an extended seven-order nonlinear state-space form as

$$\dot{\boldsymbol{x}} = \boldsymbol{f}(\boldsymbol{x}, \boldsymbol{u}_1) \tag{9}$$

where

$$x = [\, x \;\; v \;\; h_{\rho_d} \;\; i_d \;\; i_q \;\; f_d \;\; f_q \,]^T$$

$$\boldsymbol{f}(\boldsymbol{x}, \boldsymbol{u}_1) = \begin{pmatrix} v \\ \frac{1}{M_o} K_{fo} i_q - \frac{1}{M_o} F_{dis} \\ h_{\rho_d} \\ -\frac{R_{\rm so}}{L_{\rm so}} i_d + \frac{\pi}{\tau} p v i_q + \frac{1}{L_{\rm so}}(u_d - f_d) \\ -\frac{R_{\rm so}}{L_{\rm so}} i_q - \frac{\pi}{\tau} p v i_d - \frac{\pi}{\tau} p v \frac{\psi_{fo}}{L_{\rm so}} + \frac{1}{L_{\rm so}}(u_q - f_q) \\ h_d(\boldsymbol{i}, v) \\ h_q(\boldsymbol{i}, v) \end{pmatrix}.$$

It can be observed from $\boldsymbol{f}(\boldsymbol{x}, \boldsymbol{u}_1)$ that the principal factors that deteriorate the nominal system dynamics are the side-effect of the perturbed terms, i.e., $F_{\rm dis}$ of the mechanical subsystem and f_{dq} of the electrical part. The desired nominal performance can be maintained only if the disturbance can be effectively rejected.

Therefore, from the overall system point of view, the main challenges to ensure high-dynamic/precision controls of the two subsystems are similar, i.e., how to compensate the effect of parameter uncertainty and external disturbance effectively. In this paper, an integrated uncertainty/disturbance observation and compensation design method with the SOSMO will be presented in detail in the following section.

III. SOSMO-Based Uncertainty/Disturbance Compensation

A. Disturbance Compensation for the PCC With SOSMO

Our first control objective here is to design a robust current controller such that the current reference from the outer loop can be tracked fast with zero static error in the presence of parameter mismatch and unmodeled dynamics.

1) Basic Theory of the PCC: Generally, to cope with the delay effect as discussed in [14], the PCC is executed with two steps in the discrete-time domain, i.e., to predict the current of the next instant first and then to calculate the voltage commands for the next control period.

In the first step: the sampled states (i.e., the currents and velocity) and the known voltage commands of the present period are utilized to predict the currents for the next $(k+1)$th instant according to (3) as

$$\hat{\boldsymbol{i}}(k+1) = \boldsymbol{i}(k) + \boldsymbol{g}_0(\boldsymbol{i}(k), v(k))T_s + \tfrac{T_s}{L_{\rm so}}(\boldsymbol{u}_1(k) - \hat{\boldsymbol{f}}(k|k+1)) \tag{10}$$

where T_s is the sampling period (equals to the control period in this paper) of the current closed-loop.

In the second step: the voltage commands for the next $(k+1)$th period are calculated with (3) and (10) as

$$\boldsymbol{u}_1(k+1) = \tfrac{L_{\rm so}}{T_s}[\boldsymbol{i}_{\rm ref}(k+2) - \hat{\boldsymbol{i}}(k+1)] + L_{\rm so}\boldsymbol{g}_0(\hat{\boldsymbol{i}}(k+1), \hat{v}(k+1)) + \hat{\boldsymbol{f}}(k+1|k+2) \tag{11}$$

where $\hat{v}(k+1)$ is the estimated velocity of the $(k+1)$th instant, $\boldsymbol{i}_{\rm ref}(k+2)$ is the reference current of the $(k+2)$th instant, $\hat{\boldsymbol{f}}(k+1|k+2)$ and $\hat{\boldsymbol{f}}(k|k+1)$ are the observed disturbances of the $(k+1)$th and kth current-control periods, respectively.

Considering that the mechanical dynamics is generally much slower than the current dynamics, the velocity can be simply assumed varying linearly among the two-consecutive current-control periods (200 μs in this paper), i.e.,

$$\hat{v}(k+1) \approx 2v(k) - v(k-1). \tag{12}$$

In the cascaded velocity and current closed-loop control scheme, the reference currents $\boldsymbol{i}_{\rm ref}(k+2)$ are the controller output of the velocity controller and cannot be obtained in advance. Although the Lagrange interpolation method can be used to estimate $\boldsymbol{i}_{\rm ref}(k+2)$ [17], we define

$$\boldsymbol{i}_{\rm ref}(k+2) \doteq \boldsymbol{i}^*(k) \tag{13}$$

in this paper for simplicity. According to the analysis in [15], [16], and [18], as the disturbance is fully compensated, the current reference will be fully tracked/sensed after a two-control-periods delay. Therefore, the definition (13) is naturally reasonable, that is, the reference $\boldsymbol{i}^*(k)$ will be fully sensed at the $(k+2)$th instant, i.e., $\boldsymbol{i}(k+2) = \boldsymbol{i}^*(k) = \boldsymbol{i}_{\rm ref}(k+2)$.

However, the above ideal tracking performance can only be realized as the parameters in (10) and (11) are completely accurate. *Therefore, how to handle the problem of parameter mismatch effectively and so as to maintain the superior performance of the PCC is one of the main focuses of this paper.*

2) Proposed SOSMO Method: Based on the motivation of modeling the disturbance as an extended state in [9] and [27] and combining with the second-order supertwisting algorithm (STA) proposed by Levant [28], the current estimation dynamics both considering the disturbance dynamics can be developed as

$$\left.\begin{aligned}\dot{\hat{\boldsymbol{i}}} &= \boldsymbol{g}_0(\boldsymbol{i}, v) + \tfrac{1}{L_{\rm so}}(\boldsymbol{u}_1 - \hat{\boldsymbol{f}}) + \boldsymbol{z}_{11}\\ \dot{\hat{\boldsymbol{f}}} &= \boldsymbol{z}_{12}\end{aligned}\right\} \tag{14}$$

where $\boldsymbol{z}_{11}$ and $\boldsymbol{z}_{12}$ are the correction terms.

Define the current and disturbance estimation errors as

$$\left.\begin{aligned}\boldsymbol{e}_{\boldsymbol{i}} &= \boldsymbol{i} - \hat{\boldsymbol{i}}\\ \boldsymbol{e}_{\boldsymbol{f}} &= \boldsymbol{f} - \hat{\boldsymbol{f}}\end{aligned}\right\} \tag{15}$$

then the correction terms in (14) can be designed as

$$\left.\begin{aligned}\boldsymbol{z}_{11} &= \alpha_1|\boldsymbol{e}_{\boldsymbol{i}}|^{1/2}{\rm sgn}(\boldsymbol{e}_{\boldsymbol{i}})\\ \boldsymbol{z}_{12} &= \alpha_2{\rm sgn}(\boldsymbol{e}_{\boldsymbol{i}})\end{aligned}\right\} \tag{16}$$

where $\alpha_1 > 0$ and $\alpha_2 > 0$ are the gains to be designed.

Next, by subtracting (3) from (14), the error dynamics can be deduced as

$$\left.\begin{aligned}\dot{\boldsymbol{e}}_{\boldsymbol{i}} &= -\boldsymbol{z}_{11} - \tfrac{1}{L_{\rm so}}\boldsymbol{e}_{\boldsymbol{f}}\\ \dot{\boldsymbol{e}}_{\boldsymbol{f}} &= -\boldsymbol{z}_{12} - \boldsymbol{h}(\boldsymbol{i}, v)\end{aligned}\right\}. \tag{17}$$

In practical, it is reasonable to assume that the change rate of the disturbance is bounded, i.e., $|\boldsymbol{h}(\boldsymbol{i}, v)| < \Delta_0$. Then, if the gains are designed as $\alpha_1 = 1.5\sqrt{\Delta_0}$ and $\alpha_2 = 1.1\Delta_0$, both the errors $\boldsymbol{e}_{\boldsymbol{i}}$ and $\boldsymbol{e}_{\boldsymbol{f}}$ will converge to zero in finite-time simultaneously. The detailed proof of the finite-time stability characteristic of the above error dynamics (17) can be found in [28]–[30], and they are introduced in the Appendix. Thus, as the errors (15) converge to zeros, the estimated states will approximate to their actual values, i.e., $\hat{\boldsymbol{i}} \to \boldsymbol{i}$, $\hat{\boldsymbol{f}} \to \boldsymbol{f}$.

Therefore, according to (14), the *more exact current prediction* of (10) is modified as

$$\hat{\boldsymbol{i}}(k+1) = \boldsymbol{i}(k) + T_s\boldsymbol{g}_0(\boldsymbol{i}(k), v(k)) + \tfrac{T_s}{L_{\rm so}}(\boldsymbol{u}_1(k) - \hat{\boldsymbol{f}}(k|k+1)) + T_s\boldsymbol{z}_{11}(k) \tag{18}$$

and the disturbance $\hat{\boldsymbol{f}}(k+1|k+2)$ can be estimated with

$$\hat{\boldsymbol{f}}(k+1|k+2) = \hat{\boldsymbol{f}}(k|k+1) + \boldsymbol{z}_{12}(k)T_s. \tag{19}$$

After that, combining with (12), (13), (18), and (19), the *more accurate voltage commands calculation* of (11) is deduced as

$$\boldsymbol{u}_1(k+1) = \tfrac{L_{\rm so}}{T_s}[\boldsymbol{i}_{\rm ref}(k+2) - \hat{\boldsymbol{i}}(k+1)] + L_{\rm so}\boldsymbol{g}_0(\hat{\boldsymbol{i}}(k+1), \hat{v}(k+1)) + \hat{\boldsymbol{f}}(k+1|k+2) - L_{\rm so}\boldsymbol{z}_{11}(k+1) \tag{20}$$

where $\boldsymbol{z}_{11}(k+1)$ is described as

$$\boldsymbol{z}_{11}(k+1) = \alpha_1|\boldsymbol{e}_{\boldsymbol{i}}(k+1)|^{1/2}{\rm sgn}(\boldsymbol{e}_{\boldsymbol{i}}(k+1)) \tag{21}$$

$$\boldsymbol{e}_{\boldsymbol{i}}(k+1) = \boldsymbol{i}(k+1) - \hat{\boldsymbol{i}}(k+1). \tag{22}$$

Although the value of $\boldsymbol{i}(k+1)$ is not known at present, it can be replaced with the reference one of the $(k-1)$th instant as discussed in (13), so (22) can be estimated as

$$\boldsymbol{e}_{\boldsymbol{i}}(k+1) = \boldsymbol{i}^*(k-1) - \hat{\boldsymbol{i}}(k+1). \tag{23}$$

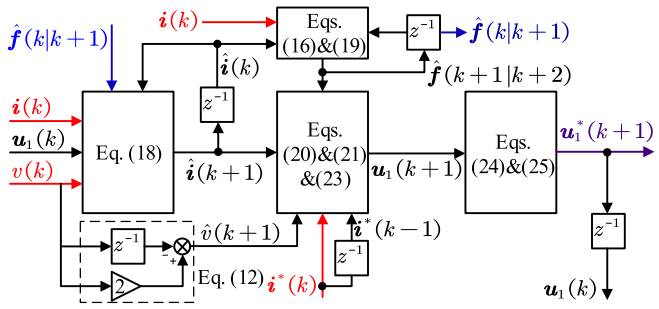

Fig. 1. Discrete diagram of the proposed robust PCC based on the SOSMO.

Therefore, accurate disturbance estimation can be obtained with (19), and then the accurate compensation for the PCC with (18) and (20) can be implemented.

In the real digital drive with the voltage-source inverter (VSI) based on the space-vector pulsewidth modulation (SVPWM) scheme, the saturation effect of the VSI should also be considered and then the actual voltage applied to the motor is given as [17]

$$\boldsymbol{u}_{1,\mathrm{ref}} = \begin{cases} \boldsymbol{u}_{1,\mathrm{ref}}(k+1) & u_{\mathrm{ref}}(k+1) \le U_{dc}/\sqrt{3} \\ \frac{U_{dc}/\sqrt{3}}{u_{\mathrm{ref}}(k+1)}\boldsymbol{u}_{1,\mathrm{ref}}(k+1) & u_{\mathrm{ref}}(k+1) > U_{dc}/\sqrt{3} \end{cases} \tag{24}$$

with

$$\begin{aligned} u_{\mathrm{ref}}(k+1) &= ||\boldsymbol{u}_{1,\mathrm{ref}}(k+1)|| \\ &= \sqrt{u_{d,\mathrm{ref}}^2(k+1) + u_{q,\mathrm{ref}}^2(k+1)} \end{aligned}$$

in which U_{dc} is the dc-link voltage of the VSI.

Meanwhile, there is difference between the measured position at the kth instant and actual one at the $(k+1)$th control period especially in a high-velocity operation. According to the basic assumption in (12), the voltage command can be further corrected as [14]

$$\boldsymbol{u}_{1,\mathrm{ref}}^{*} = \boldsymbol{u}_{1,\mathrm{ref}} e^{j(2.5\theta(k) - 1.5\theta(k-1))} \tag{25}$$

where $\theta = x\pi/\tau$ is the equivalent electrical angle.

By this time, the robust PCC against parameter mismatch and unmodeled dynamics can be realized with (12), (13), (16), (18)–(21), (23)–(25). The discrete control diagram of the proposed robust PCC is depicted in Fig. 1. As the disturbance being fully compensated in finite time, the high bandwidth and strong-robust inner current loop can be obtained, and then the current dynamics can be neglected for the outer-loop design.

B. Force Ripple Compensation With SOSMO

Generally, only the position encoder is installed for the motion systems. The velocity is not measurable but can be estimated from the differentiation of the position signal. For filtering out the high-frequency noises due to the quantization errors and the sampling noises, a simple first-order low-pass filter (LPF) is designed.

And then the velocity can be considered as an equivalent measured state, the velocity dynamic in system (8) can be simplified as a perturbed integrator with

$$\left.\begin{aligned} \dot{v} &= u_2 + \rho_d \\ \dot{\rho}_d &= h_{\rho_d} \end{aligned}\right\} \tag{26}$$

where $u_2 = \frac{1}{M_o} K_{fo} i_q$, $\rho_d = -\frac{1}{M_o} F_{\mathrm{dis}}$, and h_{ρ_d} are the control input, the disturbance, and its derivative, respectively.

To observe the disturbance ρ_d exactly in finite time, it is also necessary to model it as an extended state. According to (26), the velocity estimation dynamics can be extended as [28]

$$\left.\begin{aligned} \dot{\hat{v}} &= u_2 + \hat{\rho}_d + z_{21} \\ \dot{\rho}_d &= z_{22} \end{aligned}\right\} \tag{27}$$

where z_{21} and z_{22} are the correction terms.

Define the velocity and disturbance estimation errors as

$$\left.\begin{aligned} e_v &= v - \hat{v} \\ e_{\rho_d} &= \rho_d - \hat{\rho}_d \end{aligned}\right\} \tag{28}$$

then the correction terms can be designed as

$$\left.\begin{aligned} z_{21} &= \beta_1 |e_v|^{1/2} \mathrm{sgn}(e_v) \\ z_{22} &= \beta_2 \mathrm{sgn}(e_v) \end{aligned}\right\} \tag{29}$$

in which $\beta_1 > 0$ and $\beta_2 > 0$ are the gains to be designed.

Then, the estimation error dynamics can be deduced by subtracting (26) from (27) as

$$\left.\begin{aligned} \dot{e}_v &= -z_{21} + e_{\rho_d} \\ \dot{e}_{\rho_d} &= -z_{22} + h_{\rho_d} \end{aligned}\right\}. \tag{30}$$

Similarly, it is reasonable to assume that the change rate of disturbance $\dot{\rho}_d$ is bounded, i.e., $|\dot{\rho}_d| < \Delta_1$. Then, if the gains are designed as $\beta_1 = 1.5\sqrt{\Delta_1}$ and $\beta_2 = 1.1\Delta_1$, both the errors e_v and e_{ρ_d} will converge to zero in finite-time simultaneously. The detailed proof of the finite-time stability characteristic of the above error dynamics (30) can also be found in [28]–[30], and they are introduced in the Appendix. Thus, when the above errors converge to zeros, the estimated states will approximate to their actual values, i.e., $\hat{v} \to v$, and $\hat{\rho}_d \to \rho_d$, respectively.

Therefore, the velocity of the kth instant $\hat{v}(k)$ and the disturbance of the next velocity-control period $\hat{\rho}_d(k|k+1)$ can be estimated from (27) and (29) as follows:

$$\begin{aligned} \hat{v}(k) = v(k-1) \\ + [u_2(k-1) + \hat{\rho}_d(k-1|k) + z_{21}(k-1)]T_s \end{aligned} \tag{31}$$

$$\hat{\rho}_d(k|k+1) = \hat{\rho}_d(k-1|k) + z_{22}(k)T_s \tag{32}$$

where $\hat{\rho}_d(k-1|k)$ is the estimated mechanical disturbance in the present period. Next, according to (4) and (26), the equivalent q-axis current for compensating the disturbance of the mechanical subsystem can be deduced as

$$i_{qc}(k) = \hat{\rho}_d(k|k+1) M_o / K_{fo}. \tag{33}$$

The overall structure including the velocity-closed-loop control and the disturbance compensation is depicted in Fig. 2.

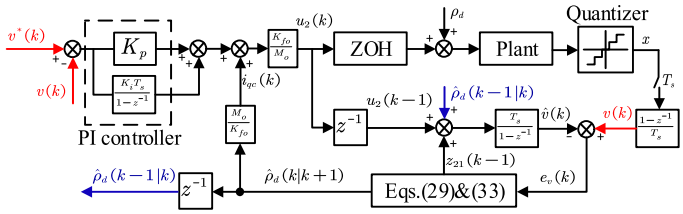

Fig. 2. Discrete implementation diagram of the velocity closed-loop control with disturbance estimation and compensation.

TABLE I
MAIN PARAMETERS OF THE TESTED PMLSM

Parameters	Values	Unit	Parameters	Values	Unit
Nominal/ Maximum thrust	600/ 1200	N	Thrust coefficient	94.2	N/A
Nominal velocity	0.6	*m/s*	Mover mass	45	kg
Stator resistance	6.5	Ω	Magnetic flux	0.24	Wb
Stator inductance	35	mH	Pole/slot number	24/18	-

IV. EXPERIMENTAL EVALUATION

A. Experimental Setup

To verify the validity of the proposed method, as depicted in Fig. 3, an air-bearing test platform driven with the surface-mounted PMLSM was built. The main parameters of the tested PMLSM is shown in Table I.

The motor was driven with a full digital power amplifier based on the 32-bit floating-point DSP TMS320F28335. The amplifier adopted a three-phase VSI with three sets of insulated-gate bipolar-transistors under the bus voltage of 100 V, which is converted from a single-phase rectifier supplied with a voltage regulator. The sampling frequency of the velocity and the current loop was equal to the switching frequency (5 kHz) in this paper. The currents of phase windings were measured through two LEM current sensors with high accuracy of $\pm 0.2\%$. For eliminating the effect of commutation spikes, the synchronous sampling technique with symmetric SVPWM was configured. To reduce the noises of sampled currents, both the repeated sampling handling in a software algorithm and the second-order Butterworth LPF in hardware circuits design were used. Then, the internal 12-bit A/D converter of the DSP was utilized to convert the currents to the digital values. The mover position was measured through a high-resolution (0.1 μm) linear scale, and the velocity was simply estimated with the backward differentiation method. The cutoff frequency was designed as 100 Hz. The interested variables were transmitted to the host computer with LabVIEW through the CAN transceiver and then were plotted again in the MATLAB. The simplified block diagram of the overall system is shown in Fig. 4.

B. Evaluation Results

Fig. 5 shows the square-wave current response of the PCC under nominal parameters with and without considering the delay compensation with (10) and (11); it can be noted that the oscillation and overshoot problem is effectively eliminated as the two-step strategy is used.

1) SOSMO for the PCC: First, the SOSMO is implemented with the PCC to test its compensation effect as the parameter mismatch exists between the controller and the actual plant in the single current closed-loop. The gains of (16) are designed as $\alpha_1 = 5, \alpha_2 = 1500$ for considering both the convergence speed and the chattering effect, which deviates from its standard design caused by the discrete implementation. Fig. 6 shows the square-wave current response of the PCC with/without the SOSMO as only the resistance mismatch ($R_s = 2R_{so}$) exists. According to (2), the disturbance of the q-axis due to the resistance mismatch can be estimated with $f_q \approx \Delta R_s i_q$ in the steady state. It can be seen from Fig. 6(a) that the static current error maintains without the disturbance compensation. Combined with the SOSMO, the current error is eliminated after 7 ms, and the estimated q-axis disturbance voltage $\hat{f}_q$ converges to its theoretical value ($\approx 1\ \mathrm{A}^* R_{so} = 6.5$ V) gradually, as shown at the bottom of Fig. 6(b).

As only the inductance mismatch ($L_s = 0.3L_{so}$) exists, the dynamic response speed of the q-axis current is largely reduced, as shown in Fig. 7(a). When considering the disturbance compensation with the SOSMO, as depicted in Fig. 7(b), the response of the q-axis current is accelerated with the settling time decreasing from 5 ms to about 3.4 ms. Thus, compared with the adaptive method [31], the SOSMO method can also maintain large inductance robustness range. Meanwhile, the observed disturbance approaches to zero as expected of (2) in the steady state, as shown at the bottom of Fig. 7(b), due to that the disturbance of q-axis can be estimated with $f_q \approx \Delta L_s \frac{d}{dt} i_q$ during the transient process. According to (2), the inductance mismatch will also lead to the d-axis disturbance, which is dominantly relative to the mover velocity and the q-axis current. Under this single current closed-loop, the effect of inductance mismatch on the d-axis current tracking error is not large enough to be observed. Nevertheless, the corresponding results will be shown in Fig. 8 under higher velocity and higher q-axis current.

To further verify the compensation effect of the SOSMO for the PCC, the condition that all the three parameters vary from their nominal one (e.g., $R_s = 2R_{so}, L_s = 0.3L_{so}, \psi_f = 2\psi_{fo}$) is also tested in the velocity closed-loop. The gains of the velocity PI-controller were designed as $k_p = 5, k_i = 0.015$, where the controller structure is $G_{PI} = k_p + k_i/s$. The velocity command is designed as a trapezoidal wave with a high acceleration of 4 m/s^2 and a high velocity of 0.4 m/s.

Without considering the disturbance compensation, there exists static current error of the q- and d-axis both in the acceleration/deceleration and constant velocity phase, as shown in Fig. 8. As the mover accelerates gradually, as illustrated in Fig. 8(a), the actual q-axis current increases gradually due to that the effect of flux mismatch is coupled with the velocity according to (2). For the same reason, both the resistance and flux mismatch lead to the static current error of the q-axis when the velocity is constant. The nonzero q-axis current command is caused by the cable force, which is equal to an external light load. Simultaneously, according to (2), the d-axis disturbance can also be estimated with $f_d \approx -\frac{\pi}{\tau} pv\Delta L_s i_q$. During the acceleration phase, the disturbance will contribute to the increasing d-axis current, which is proportional to the mover velocity. Then, in

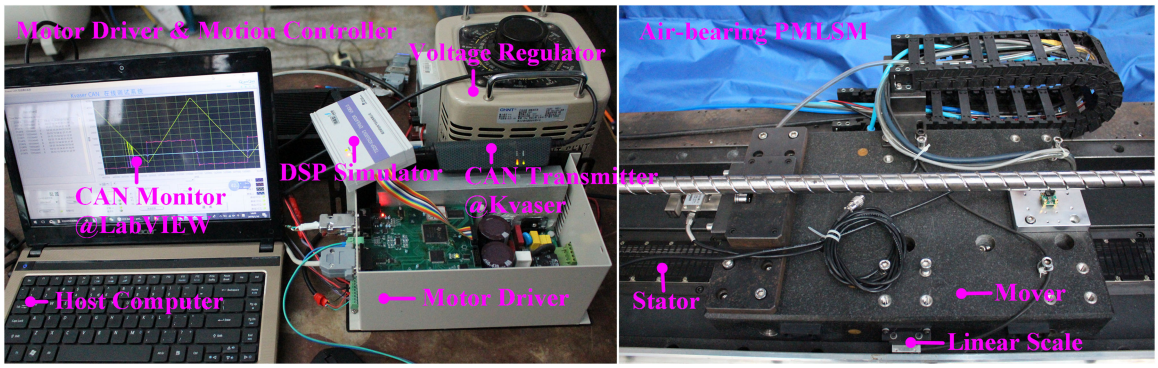

Fig. 3. Air-bearing test-platform driven with surface-mounted PMLSM.

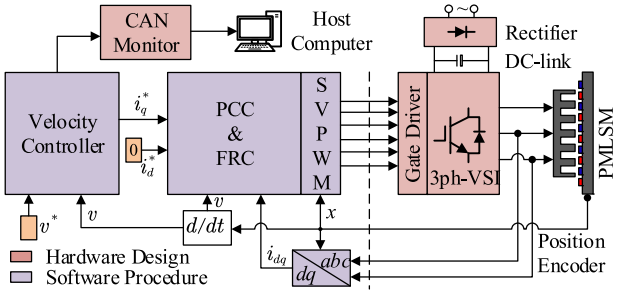

Fig. 4. Schematic diagram of the velocity and current double-closed-loop control system for the PMLSM.

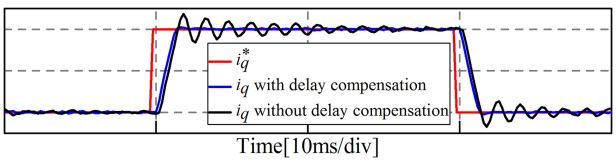

Fig. 5. Square-wave current response of the PCC with and without considering delay compensation.

the constant velocity phase, the higher velocity and the little q-axis current will also lead to the static error. The difference between the acceleration and deceleration phases is caused by the different characteristics of the cable force.

When the SOSMO is configured, the current error is eliminated in all the three phases [see Fig. 8(b)]. The bottom one of Fig. 8(b) shows the estimated disturbance. As for the q-axis, at the initial moment of the acceleration phase [e.g., A→B in Fig. 8(b)], $\hat{f}_q$ steps to about 14 V caused by the effect of resistance mismatch ($R_s = 2R_{so}$) and the step current response (about 2.1 A), which is almost equal to the theoretical value 13.65 V (2.1A$^*R_{so}$ = 13.65 V). As the mover moves with a constant velocity [e.g., D→E in Fig. 8(b)], the correctness of $\hat{f}_q$ can also be verified with the velocity and the flux difference. Simultaneously, the correctness of $\hat{f}_d$ can also be evaluated with (2).

Therefore, the validity of the SOSMO can be verified both in the current and velocity closed-loops as the three parameters vary from its nominal values. For limited page, the experimental results with underestimated resistance/flux and overestimated inductance are not listed here.

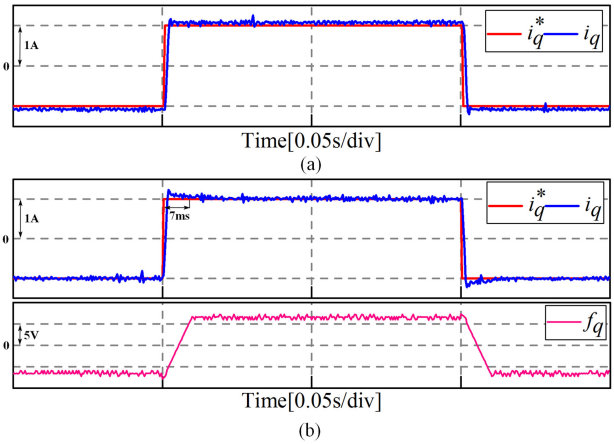

Fig. 6. Square-wave current response of the PCC. (a) Without disturbance compensation. (b) With the SOSMO as only the resistance mismatch ($R_s = 2R_{so}$) exists and the estimated q-axis disturbance.

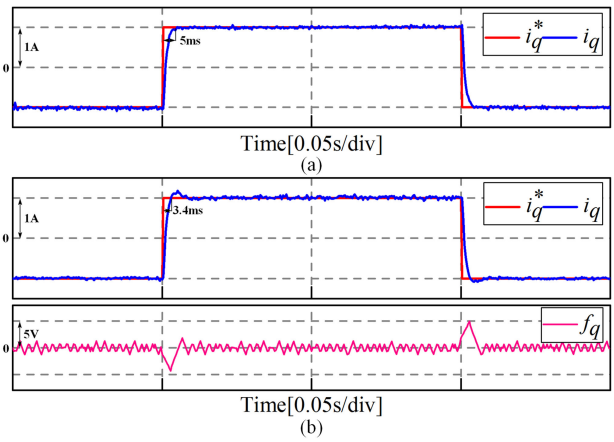

Fig. 7. Square-wave current response of the PCC. (a) Without disturbance compensation. (b) With the SOSMO as only the inductance mismatch ($L_s = 0.3L_{so}$) exists and the estimated q-axis disturbance.

2) SOSMO for the Force Ripple Compensation: Second, the SOSMO is also designed here to observe the force ripple. At a high velocity, the effect of force ripple on the velocity fluctuation will be deteriorated due to the inertia-filter role of the mechanical subsystem. Thus, the velocity command is designed here as a trapezoidal wave with a low acceleration of 0.2 m/s^2

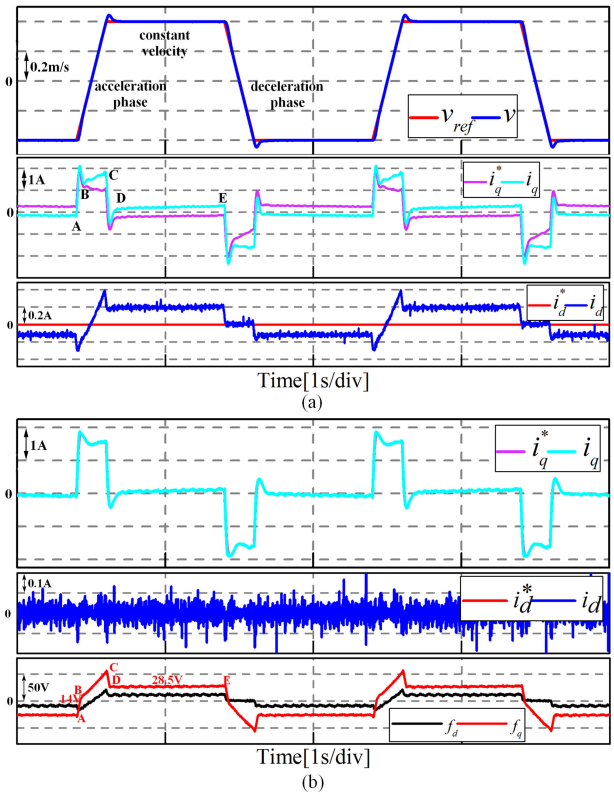

Fig. 8. (a) Trapezoidal-wave velocity response and the corresponding current command and its response. (b) Estimated disturbance of the q- and d-axis, where the mismatch ($R_s = 2R_{\rm so}, L_s = 0.3L_{\rm so}, \psi_f = 2\psi_{fo}$) exists.

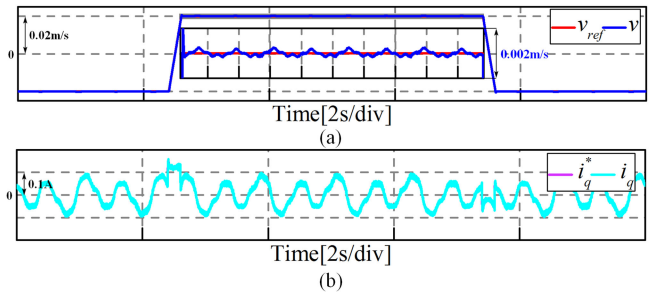

Fig. 9. (a) Simulated trapezoidal-wave velocity response. (b) Corresponding q-axis current command and its response without the force ripple compensation.

and a low velocity of 0.02 m/s to clearly evaluate the effectiveness of the proposed method. The SOSMO gains of (29) are designed as $\beta_1 = 5, \beta_2 = 15$, which deviates from its standard design caused by the discrete implementation. For verifying the correctness of the force ripple estimation, the finite-element analysis results are first modeled in the simulation model under Simulink@MATLAB using the curve-fitting method, and as shown in our previous work [26], the detent force can be presented as

$$F_d = 2.29\sin\left(\tfrac{x}{\tau}\pi\right) + 6.27\sin\left(2\tfrac{x}{\tau}\pi\right) + 1.01\sin\left(4\tfrac{x}{\tau}\pi\right) + 0.6\sin\left(8\tfrac{x}{\tau}\pi\right)\,[N]$$

where only the main harmonic components are considered.

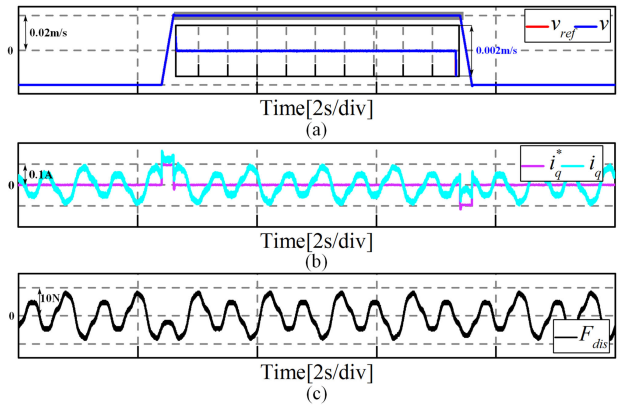

Fig. 10. (a) Simulated trapezoidal-wave velocity response. (b) Corresponding q-axis current command and its response with the force ripple compensation. (c) Observed force ripple.

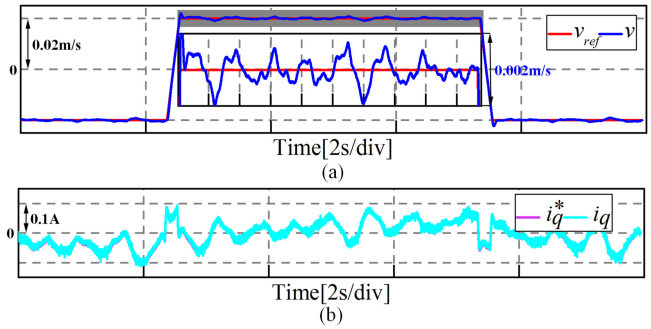

Fig. 11. (a) Trapezoidal-wave velocity response. (b) Corresponding q-axis current command and its response without the force ripple compensation.

Fig. 9 shows the simulated velocity and q-axis current response as the SOSMO is not configured. It can be noted from Fig. 9(a) that there exists periodical velocity fluctuation that is consistent with the characteristic of the detent force. Simultaneously, the current command ripple, as shown in Fig. 9(b), also indicates the effect of detent force on the velocity.

As the compensation current (33) is injected, the velocity ripple has been reduced effectively, as depicted in Fig. 10(a), and the almost constant current command of Fig. 10(b) in the constant velocity phase also reflects the validity of the method. The estimated disturbance is approximately consistent with the modeled detent force.

Then, to further evaluate the effectiveness of the SOSMO on the remaining force ripple, the proposed method is also designed in the real digital system. As the force ripple is not considered, there exists obvious velocity fluctuation ($\pm 5\%$), as shown with the magnified picture in Fig. 11(a). The actual velocity ripple can also be indirectly reflected with the ripple of the velocity controller output, i.e., i_q^* in Fig. 11(b). In general, to demonstrate the effect of force ripple on the velocity clearly, a lower velocity controller bandwidth should be designed. However, considering the velocity response performance, the velocity controller was designed with a medium bandwidth, that is to say, the closed-loop control can also suppress the force ripple to some extent. Nevertheless, the effectiveness of the SOSMO on the force rip-

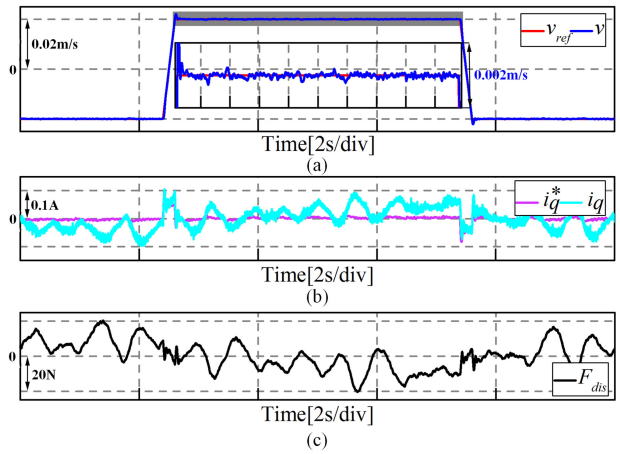

Fig. 12. (a) Trapezoidal-wave velocity response. (b) Corresponding q-axis current command and its response with the force ripple compensation. (c) Observed force ripple.

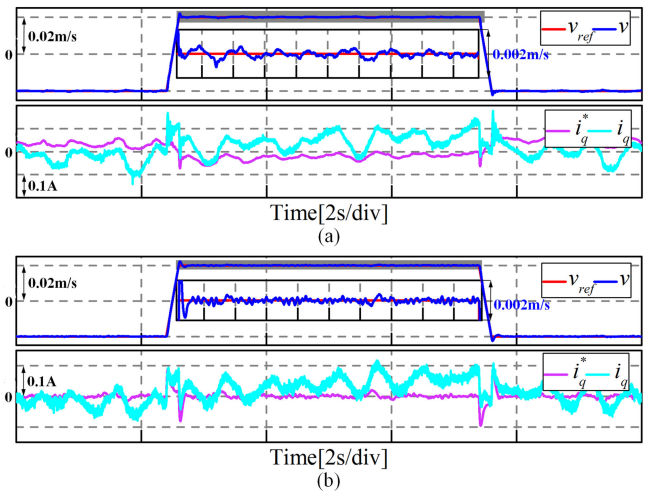

Fig. 13. Trapezoidal-wave velocity response and the corresponding q-axis current command and its response (a) without compensation and (b) with compensation for both the parameter mismatch ($R_s = 5R_{\rm so}, L_s = 0.3L_{\rm so}, \psi_f = 5\psi_{fo}$) and the force ripple.

ple suppression can also be verified, as shown in Fig. 12 and described as follows.

As depicted in Fig. 12(a), while the compensation current (33) is added, the velocity is greatly smoothed and the velocity fluctuation is reduced to about $\pm 0.6\%$, which is just about 12% of the results in Fig. 11(a). Although it can be noted that the q-axis current response seems to be similar with/without utilizing the SOSMO, there exists little difference that cannot be clearly identified due to the lower compensation current, which was caused by the higher thrust coefficient and lower force ripple, and the inevitably existing current sampling noises. The validity can also be reflected with the smooth current command of the velocity controller, i.e., i_q^* in Fig. 12(b). The relation between the current command, the actual current response, and the compensation current is $i_q = i_q^* + i_{qc}$, which can also be observed from the antiphase relation among the compensated current in Fig. 12(a) and the force ripple in Fig. 12(b). Fig. 12(c) shows the estimated force ripple, and it can be noted that it mainly comprises the position-dependent periodical component and the slowly varying part, which can be seen as thrust ripple and cable force, respectively.

Therefore, according to the simulation and experimental results, the SOSMO can estimate the main detent force and the remaining force ripple including the cable force and the effect of mechanical parameter variation and then the effect of force ripple on the velocity fluctuation can be effectively suppressed.

3) SOSMO for the Overall System Disturbance Compensation: Third, the SOSMO is utilized here to observe both the disturbance of parameter mismatch and the force ripple. To clearly show the compensation effect of SOSMO on both the PCC and the force ripple, the velocity is designed same as Fig. 11, but the parameters in the controller vary to ($R_s = 5R_{\rm so}, L_s = 0.3L_{\rm so}$, and $\psi_f = 5\psi_{fo}$). As shown in Fig. 13(b), the velocity fluctuation is also reduced greatly compared with Fig. 12(a), where the parameter of the PCC is nominal. The bottom one of Fig. 13(a) depicts the current command and its response without compensation, where the constant error exists compared with Fig. 12(b). The approximately same current response of the bottom one of Fig. 13(b) compared with Fig. 12(b) verifies that the effect of parameter mismatch on the PCC is almost eliminated. The little difference of velocity ripple between Fig. 13(a) and Fig. 11(a) is caused by the effect of flux mismatch with a constant velocity.

Therefore, with the SOSMO, the effect of parameter mismatch on the PCC and the force ripple on the velocity response can be effectively compensated.

V. Conclusion

In this paper, an integrated disturbance/uncertainty compensation method for the PMLSM-driven stage based on the SOSMO was proposed. An extended state model was established for considering the disturbance dynamics due to the parameter mismatch and external force ripple. This modification eliminates the assumption that the disturbance is slowly varying, and then more accurate disturbance can be estimated. The SOSMO can estimate both the disturbance of parameter mismatch and the external force ripple, and then the superior performance of PCC was maintained and the velocity fluctuation was reduced. Hence, the uncertainty/disturbance of the overall system was compensated simultaneously, and then the high-dynamic and low-fluctuation velocity response was obtained. Experimental results under the cascaded velocity/current double-closed-loop with electrical parameter mismatch and force ripple have both verified its effectiveness. In the future, the detailed parameter design for the SOSMO and the effect of mechanical parameter mismatch will be further studied.

Appendix

The STA can be presented as [28]

$$\begin{aligned} \dot{x}_1 &= -k_1 |x_1|^{1/2} \mathrm{sgn}(x_1) + x_2 + \rho_1(x,t) \\ \dot{x}_2 &= -k_2 \mathrm{sgn}(x_1) + \rho_2(x,t) \end{aligned} \tag{34}$$

where x_1 and x_2 are the scalar state variables, k_1 and k_2 are the gains to be designed, and ρ_1 and ρ_2 are the perturbation terms. Supposed that the perturbation terms of system (34) are globally bounded with

$$\rho_1(x,t) = 0, |\rho_2(x,t)| < L \tag{35}$$

where the constant $L > 0$.

Select the vector $\zeta^T = [\,\zeta_1\ \zeta_2\,]^T = [\,|x_1|^{1/2}\mathrm{sgn}(x_1)\ x_2\,]$, and then its derivatives can be given by

$$\dot{\zeta} = \frac{1}{|\zeta_1|}A\zeta, A = \begin{bmatrix} -\frac{1}{2}k_1 & \frac{1}{2} \\ -k_2 & 0 \end{bmatrix} \tag{36}$$

where $|\zeta_1| = |x_1|^{1/2}$. As presented in [30, Th. 2], for any positive constant L, there exist gains $k_1, k_2 > 0$ such that the origin $x = 0$ is a robust and globally finite-time stable equilibrium point. Moreover, there exists a positive and symmetric definite matrix P such that $V(x) = \zeta^T P\zeta$ is a quadratic, strict, and robust Lyapunov function for the perturbed system, satisfying

$$\dot{V} = -|x_1|^{-1/2}\zeta^T Q_R \zeta \tag{37}$$

almost everywhere, where Q_R is symmetric and positive definite matrix and fulfill $A^T P + PA = -Q_R$. Furthermore, the system state starting at x_0 will converge to the equilibrium point ($x = 0$) in a finite time smaller than

$$T_0 = \frac{2\lambda_{\max}\{P\}}{\lambda_{\min}^{1/2}\{P\}\lambda_{\min}\{Q_R\}}V^{1/2}(x_0). \tag{38}$$

REFERENCES

[1] K. Cho, J. Kim, and S. B. Choi, "A high-precision motion control based on a periodic adaptive disturbance observer in a PMLSM," *IEEE/ASME Trans. Mechatronics*, vol. 20, no. 5, pp. 2158–2171, Oct. 2015.

[2] K. K. Tan, H. Dou, Y. Chen, and T. H. Lee, "High precision linear motor control via relay-tuning and iterative-learning based on zero-phase filtering," *IEEE Control Syst. Technol.*, vol. 9, no. 2, pp. 244–253, Mar. 2011.

[3] F. J. Lin, J. C, Hwang, P. H. Chou, and Y. C. Hung, "FPGA-based intelligent-complementary sliding-mode control for PMLSM servo-drive system," *IEEE Trans. Power Electron.*, vol. 25, no. 10, pp. 2573–2587, Oct. 2010.

[4] T.-S. Hwang, and J.-K. Seok, "Observer-based ripple force compensation for linear hybrid stepping motor drives," *IEEE Trans. Ind. Electron.*, vol. 54, no. 5, pp. 2417–2424, Jul. 2007.

[5] H. Karimi, S. Vaez-Zadeh and F. R. Salmasi, "Combined vector and direct thrust control of linear induction motors with end effect compensation," *IEEE Trans. Energy Convers.*, vol. 31, no. 1, pp. 196–205, Oct. 2015.

[6] M. A. M. Cheema, J. E. Fletcher, M. F. Rahman, and D. Xiao, "Optimal, combined speed, and direct thrust control of linear permanent magnet synchronous motors," *IEEE Trans. Energy Convers.*, vol. 31, no. 3, pp. 947–958, Sep. 2016.

[7] L. Harnefors and H.-P. Nee, "Model-based current control of AC machines using the internal model control method," *IEEE Trans. Ind. Appl.*, vol. IE-34, no. 1, pp. 133–141, Jan./Feb. 1998.

[8] S. Li and Z. Liu, "Adaptive speed control for permanent magnet synchronous motor system with variations of load inertia," *IEEE Trans. Ind. Electron.*, vol. 56, no. 8, pp. 3050–3059, Aug. 2009.

[9] X. Zhang, B. Hou, and Y. Mei, "Deadbeat predictive current control of permanent-magnet synchronous motors with stator current and disturbance observer," *IEEE Trans. Power Electron.*, vol. 32, no. 5, pp. 3818–3834, May 2017.

[10] B. Wang, X. Chen, Y. Yu, G. Wang, and D. Xu, "Robust predictive current control with online disturbance estimation for induction machine drives," *IEEE Trans. Power Electron.*, vol. 32, no. 6, pp. 4663–4674, Jun. 2017.

[11] D. Q. Dang, M. S. Rafaq, H. H. Choi, and J.-W. Jung, "Online parameter estimation technique for adaptive control applications of interior PM synchronous motor drives," *IEEE Trans. Ind. Electron.*, vol. 63, no. 3, pp. 1438–1449, Mar. 2016.

[12] Y. A.-R. I. Mohamed and E. F. El-Saadany, "An improved deadbeat current control scheme with a novel adaptive self-tuning load model for a three-phase PWM voltage-source inverter," *IEEE Trans. Ind. Electron.*, vol. 54, no. 2, pp. 747–759, Apr. 2007.

[13] X.-H. Jin, Y, Zhang, and D.-G. Xu, "Static current error elimination algorithm for induction motor predictive current control," *IEEE Access*, vol. 5, pp. 15250–15209, 2017.

[14] K.-H. Kim and M.-J. Youn, "A simple and robust digital current control technique of a PM synchronous motor using time delay control approach," *IEEE Trans. Power Electron.*, vol. 16, no. 1, pp. 72–82, Jan 2001.

[15] Y. A.-R. I. Mohamed and E. F. El-Saadany, "A current control scheme with an adaptive internal model for torque ripple minimization and robust current regulation in PMSM drive system," *IEEE Trans. Energy Convers.*, vol. 23, no. 1, pp. 92–100, Mar. 2008.

[16] B. Wang, X. Chen, Y. Yu, G. Wang, and D. Xu, "Robust predictive current control with online disturbance estimation for induction machine drives," *IEEE Trans. Power Electron.*, vol. 32, no. 6, pp. 4663–4674, Jun. 2017.

[17] M. Abdelrahem, C. Hackl, Z. Zhang, and R. Kennel, "Robust predictive control for direct-driven surface-mounted permanent-magnet synchronous generators without mechanical sensors," *IEEE Trans. Energy Convers.*, vol. 33, no. 1, pp. 179–189, 2017, doi: 10.1109/TEC.2017.2744980.

[18] B. Wang, Z. Dong, Y. Yu, G. Wang, and D. Xu, "Static-errorless deadbeat predictive current control using second-order sliding-mode disturbance observer for induction machine drives," *IEEE Trans. Power Electron.*, vol. 33, no.3, pp. 2395–2403, Apr. 2017.

[19] Y. Jiang, W. Xu, C. Mu, and Y. Liu, "Improved deadbeat predictive current control combined sliding mode strategy for PMSM drive system," *IEEE Trans. Veh. Technol.*, vol. 67, no. 1, pp. 251–263, 2017, doi: 10.1109/TVT.2017.2752778.

[20] Y. M. Li and Q. S. Xu, "Design and robust repetitive control of a new parallel-kinematic XY piezostage for micro/nanomanipulation," *IEEE/ASME Trans. Mechatron.*, vol. 17, no. 6, pp. 1120–1132, Dec. 2012.

[21] K. K. Tan, H. F. Dou, Y. Q. Chen, and T. H. Lee, "High precision linear motor control via relay-tuning and iterative learning based on zero-phase filtering," *IEEE Trans. Control Syst. Technol.*, vol. 9, no. 2, pp. 244–253, Mar. 2001.

[22] L. Lu, Z. Chen, B Yao, and Q. Wang. "Desired compensation adaptive robust control of a linear-motor-driven precision industrial gantry with improved cogging force compensation," *IEEE/ASME Trans. Mechatronics*, vol. 13, no. 6, pp. 617–624, Dec. 2008.

[23] K. K. Tan, S. N. Huang and T. H. Lee, "Robust adaptive numerical compensation for friction and force ripple in permanent magnet linear motors," *IEEE Trans. Magn.*, vol. 38, no. 1, pp. 221–228, Jan. 2002.

[24] Y.-W. Zhu, S.-M. Jin, K.-S. Chung, and Y.-H. Cho, "Control-based reduction of detent force for permanent magnet linear synchronous motor," *IEEE Trans. Magn.*, vol. 45, no. 6, pp. 2827–2830, Jun. 2009.

[25] L. Bascetta, P. Rocco, and G. Magnani, "Force ripple compensation in linear motors based on closed-loop position-dependent identification," *IEEE/ASME Trans. Mechatronics*, vol. 15, no. 3, pp. 349–359, Jun. 2010.

[26] M. Y. Wang, L. Y. Li, and D. H. Pan, "Detent force compensation for PMLSM systems based on structural design and control method combination," *IEEE Trans. Ind. Electron.*, vol. 62, no. 11, pp. 6845–6854, Nov. 2015.

[27] M. Guermouche, S. A. Ali, and N. Langlois, "Super-twisting algorithm for DC motor position control via disturbance observer," *IFAC-PapersOnLine*, vol. 48, no. 30, pp. 43–48, 2015.

[28] A. Levant, "Higher-order sliding modes, differentiation and output-feedback control," *Int. J. Control*, vol. 76, no. 9/10, pp. 924–941, 2003.

[29] A. Chalanga, S. Kamal, L. M. Fridman, B. Bandyopadhyay, and J. A. Moreno, "Implementation of super-twisting control super-twisting and higher order sliding-mode observer-based approaches," *IEEE Trans. Ind. Electron.*, vol. 63, no. 6, pp. 3677–3685, Jun. 2016.

[30] J. A. Moreno and M. Osorio, "Strict Lyapunov functions for the super-twisting algorithm," *IEEE Trans. Autom. Control*, vol. 57, no. 4, pp. 1035–1040, Apr. 2012.

[31] R. Yang, M. Y. Wang, L. Y. Li, C. M. Zhang, and J. L. Jiang, "Robust predictive current control with variable-gain adaptive disturbance observer for PMLSM," *IEEE Access*, vol. 6, no. 99, pp. 13158–13169, Mar. 2018.

Rui Yang was born in Hubei, China. He received the B.E. degree in electrical engineering in 2015 from the Harbin Institute of Technology, Harbin, China, where he is currently working toward the Ph.D. degree in electrical engineering.

His research interests include linear motor drive and control, predictive current control, adaptive control, and sliding-mode control.

Mingyi Wang was born in Jilin, China. He received the B.E., M.E., and Ph.D. degrees in electrical engineering from the Harbin Institute of Technology (HIT), Harbin, China, in 2009, 2011, and 2016, respectively.

He is currently with the Institute of Electromagnetic and Electronic Technology, HIT. His research interests include motor drive control, power electronic applications, and magnetic levitation.

Liyi Li (SM'17) received the B.E., M.E., and D.E. degrees from the Harbin Institute of Technology (HIT), Harbin, China, in 1991, 1995, and 2001, respectively.

Since 2004, he has been a Professor with the School of Electrical Engineering and Automation, HIT. In 2013, he became a "Yangtze Fund Scholar" Distinguished Professor, and his work is currently supported by the National Science Fund for Distinguished Young Scholars. He has authored or coauthored more than 110 technical papers and is the holder of 50 patents. His research interests include design, drive and control of linear motors, design and drive of high-speed/power density permanent magnet machines.

Yiming Zenggu was born in Sichuan, China. He received the B.E. degree in electrical engineering from the Hefei University of Technology, Hefei, China, in 2017. He is currently working toward the M.E. degree in electrical engineering in the Harbin Institute of Technology, Harbin, China.

His research interests include linear motor drive and control, extended Kalman filter, and active disturbance rejection control.

Jialin Jiang was born in Jiamusi, China. He received the B.E. degree in electrical engineering in 2017 from the Harbin Institute of Technology, Harbin, China, where he is currently working toward the M.E. degree in electrical engineering.

His research interests include linear motor drive and control and sliding-mode control.